Phonon Angular Momentum Generation in Single-Stranded Helix Structure

Hong Sun(孙鸿)[1†], Jiaqi Chen(陈佳麒)[1†], Qingxuan Wang(王庆轩)[1], Xiaoliang Zeng(曾小亮)[2], Jun Zhou(周俊)[1*], and Lifa Zhang(张力发)[1*]

[1]*Ministry of Education Key Laboratory of NSLSCS, Phonon Engineering Research Center of Jiangsu Province, Center for Quantum Transport and Thermal Energy Science, Institute of Physics Frontiers and Interdisciplinary Sciences, School of Physics and Technology, Nanjing Normal University, Nanjing 210023, China*

[2]*Shenzhen Institute of Advanced Electronic Materials, Shenzhen Institutes of Advanced Technology, Chinese Academy of Sciences, Shenzhen 518055, China*

(Received 16 June 2025; accepted manuscript online 4 August 2025)

The experimental realization of observable phonon angular momentum (PAM) in feasible systems using relatively simple methods remains a critical challenge. Motivated by the chiral-induced spin selectivity effect, this study explores the generation of PAM during the transport of electrically driven polarons along a single-stranded helix structure. We demonstrate that the motion of a polaron under an applied electric field inherently induces a finite PAM, exhibiting drift-locked behavior between the PAM and the polaron. By analyzing the time evolution of PAM distribution at each site, we identify the observed PAM as a natural consequence of coherent superposition between lattice waves, in which the chiral structure selectively determines the direction of induced PAM. Furthermore, we examine the roles of two types of electron–phonon interactions and structural periodicity in modulating PAM. These findings highlight the potential of chiral molecules as platforms for PAM generation and offer new insights into developing phonon-spin-based devices for information processing and transmission.

DOI: 10.1088/0256-307X/42/9/090711 CSTR: 32039.14.0256-307X.42.9.090711

1. Introduction. Phonons, quantized lattice vibrations, have traditionally been regarded as quasiparticles that carry only energy and quasi-momentum. However, this perspective has evolved with the proposal of chiral phonons,[1–3] which possess nonzero angular momentum due to circularly rotating atomic motion around equilibrium positions, akin to the definition of orbital angular momentum of atoms. To date, phonon angular momentum (PAM) has reinvigorated the field of condensed matter physics, not only giving rise to many novel phonon-driven phenomena[4–6] but also significantly impacting the thermal,[7–9] electrical,[10–12] optical,[13] and magnetic[14–16] properties of materials. Nevertheless, under currently available laboratory conditions, the efficient and reliable generation of PAM remains a critical issue that urgently requires attention and resolution. Two primary factors may account for this challenge: (i) the constraints imposed by crystal symmetry and (ii) the difficulty of efficiently controlling phonons directly. For one thing, PAM arising directly from atomic motion within the lattice is strictly governed by crystal symmetry and can only exist when time-reversal symmetry is broken.[17] For another thing, as neutral particles, phonons cannot be directly controlled using conventional methods such as electric or magnetic fields like electrons. Consequently, while theoretical advancements in PAM have been substantial, practical challenges persist in terms of experimental observation, device design, and application development.

Considerable research has already been conducted on addressing this challenging problem. The earliest endeavor can be traced back to those pioneering works,[1,18–20] where the time-reversal symmetry of the lattice was broken via the introduction of a phenomenological spin–phonon interaction[21,22] induced by an external magnetic field, thereby giving rise to a finite PAM. However, owing to the incomplete understanding of lattice dynamics in magnetic fields and the constraints of the models, the application scope and parameter selection of the key spin–phonon interaction involve a degree of subjectivity, which ultimately lead to the fact that the calculated results often fail to fully capture the generation of PAM in real experiments, further complicating the selection of suitable experimental materials. Furthermore, in addition to artificially breaking symmetry, other attempts[23–25] have also been investigated, such as exploring the possibility of achieving nonzero PAM through the mutual conversion of angular momentum within many-body systems. Among these efforts, the most representative work is to provide a rational explanation for the ultrafast demagnetization phenomenon,[26] where the angular momentum lost by the spin system is found to be transferred to phonons. Nevertheless, it should be mentioned that the PAM generated in this manner exhibits a transient behavior and cannot persist over extended periods. Within picoseconds timescales, it spon-

†These authors contributed equally to this work.
*Corresponding authors. Email: zhoujunzhou@njnu.edu.cn; phyzlf@njnu.edu.cn
© 2025 Chinese Physical Society and IOP Publishing Ltd. All rights, including for text and data mining, AI training, and similar technologies, are reserved.

taneously decoheres, converting into thermal energy and dissipating. Consequently, despite the successful excitation of phonon modes with pronounced PAM using specific methods, extending the effective lifetime of such PAM remains a pressing scientific challenge.

Recent advancements [27–29] concerning the generation of PAM from chiral structural materials may offer promising insights into addressing this challenge. In these studies, the selective effect of chiral structures on chiral phonon transport is crucial for generating continuous PAM. Such phenomena where angular momentum is restricted by chiral structure during transport lead us to contemplate another well-recognized phenomenon: the chiral-induced spin selection (CISS) effect. [30–32] In this effect, electron transmission through a chiral molecule shows a preference for one spin orientation over the other. A natural question arises: can additional PAM be induced in chiral molecules during the CISS process? Given that this system exhibits strong electron–phonon interactions, electrons do not exist independently but instead couple with surrounding lattice distortions to form spatially localized polarons. What role does the polaron play in PAM generation? Moreover, what roles do recently discovered diverse electron–phonon interactions, such as electron–chiral phonon (ECP) interactions, [33] contribute to this mechanism? These questions remain unanswered as of now.

In this Letter, we investigate the generation of PAM in polaron transport by employing a chiral chain model with spin-related dynamics. The results show that the direction of the induced PAM is opposite to the drift velocity of the polaron, which can ultimately be attributed to the coherent superposition between lattice waves. In contrast to previous studies [34,35] that predominantly focused on single electrons as carriers, in our model, the existence of a stable polaron is a necessary condition for inducing extra PAM. Moreover, the conventional electron–phonon interaction is found to play a more significant role in this process compared to the ECP interaction. Specifically, the former determines the size and drift velocity of the polaron, thereby further influencing the resulting PAM. While the latter one, owing to the mismatch in time scales between polaron motion and lattice response, manifests only as a periodic disturbance applied to the induced PAM. Finally, we discuss the impact of structural periodicity, which indicates that increasing the number of atoms in a single helical chain enhances the generation efficiency of PAM. However, this may potentially exert an adverse effect on spin flipping.

2. Theoretical Model. We depict the chiral DNA molecule by using the following Su–Schrieffer–Heeger model (shown in Fig. 1):

$$H = H_{\rm el} + H_{\rm ph} + H_{\rm ECP}, \tag{1}$$

where $H_{\rm el}$ represents the electron's Hamiltonian, including the kinetic, potential, and spin–orbit coupling (SOC) energies of the electrons. Through the standard second quantization procedure, $H_{\rm el}$ can be written as: [36]

$$\begin{aligned} H_{\rm el} = & \sum_{js} \varepsilon_j c^{\dagger}_{j,s} c_{j,s} - \sum_{js} t_j (c^{\dagger}_{j,s} c_{j+1,s} + c^{\dagger}_{j+1,s} c_{j,s}) \\ & - {\rm i}t_{\rm SO} \sum_{j} ({\rm e}^{-{\rm i}\varphi_j} c^{\dagger}_{j,\uparrow} c_{j,\downarrow} + {\rm e}^{{\rm i}\varphi_j} c^{\dagger}_{j,\downarrow} c_{j,\uparrow}) \\ & + t_{\rm SI} \sum_{j} ({\rm e}^{-{\rm i}\varphi_j} c^{\dagger}_{j+1,\uparrow} c_{j,\downarrow} - {\rm e}^{-{\rm i}\varphi_j} c^{\dagger}_{j,\uparrow} c_{j+1,\downarrow} \\ & + {\rm e}^{{\rm i}\varphi_j} c^{\dagger}_{j,\downarrow} c_{j+1,\uparrow} - {\rm e}^{{\rm i}\varphi_j} c^{\dagger}_{j+1,\downarrow} c_{j,\uparrow}). \end{aligned} \tag{2}$$

The operator $c^{\dagger}_{j,s}$ ($c_{j,s}$) creates (annihilates) a spin-s electron at site j within the molecule. The first term represents the on-site energy of the electrons, whereas the second term describes the hopping between neighboring sites. For the sake of generality, we assume the on-site energy ε_j to be zero as a reference and define the hopping integral t_j as $t_0 + (-1)^j t_{\rm e} - \alpha d_{j,j+1}$ with t_0 being the nearest neighbor transfer integral for a uniform lattice structure, $t_{\rm e}$ being the symmetry-breaking parameter introduced to lift the ground-state degeneracy, $d_{j,j+1}$ being the variation of the bond length between jth and $j+1$th sites induced by phonon, and α being the conventional electron–phonon interaction constant. Furthermore, the third and fourth terms represent an effective SOC originating from the helix symmetry of the molecule, [37] where $t_{\rm SO}$ ($t_{\rm SI}$) denotes the on-site (intersite) SOC strength, $\varphi_j = 2\pi j/N_0$ is the helical angle of site j, and N_0 is the number of sites in one period.

Given the large mass of bases, we employ the classical theory to characterize the lattice vibrations,

$$H_{\rm ph} = \sum_j \frac{1}{2} M v_j^2 + \sum_{j,j'} \frac{1}{2} u_j^{\rm T} K_{j,j'} u_{j'} \sum_j \frac{1}{2} u_j^{\rm T} K_{\rm onsite} u_j, \tag{3}$$

where M is the single site's mass, $u_j = (u_{j_x}, u_{j_y}, u_{j_z})^{\rm T}$ is the displacement vector of the jth site, and v_j is the corresponding velocity. Rather than merely concentrating on the vibration of isostatic springs along the bonding direction, here we introduce a force constant matrix $K_{j,j'}$ that preserves chiral symmetry. This enables a more comprehensive investigation of phonon vibration behaviors in all directions. Moreover, a really small on-site term $K_{\rm onsite}$ is incorporated to break the translational symmetry of the lattice system, thereby determining the lattice configuration. Such on-site term can be interpreted as a damping effect induced by the environmental conditions surrounding the DNA molecule in practical scenarios.

The last term in Eq. (1), $H_{\rm ECP} \propto \boldsymbol{S}_j \cdot \boldsymbol{L}_j$, represents the spin-rotation interaction [38] between ECP, which has been proven to play a pivotal role in high temperature superconductivity and spin transport. [35,39] For simplicity, we consider only the case in which an ion rotates around an electron, as derived in Ref. [33]. Within the framework of tight-binding approximation, the ECP interaction is finally described as the following effective model:

$$H_{\rm ECP} = g \sum_{\lambda j} L^{\lambda}_j (c^{\dagger}_{j,\uparrow}\ c^{\dagger}_{j,\downarrow}) \sigma_{\lambda} (c_{j,\uparrow}\ c_{j,\downarrow})^{\rm T}, \tag{4}$$

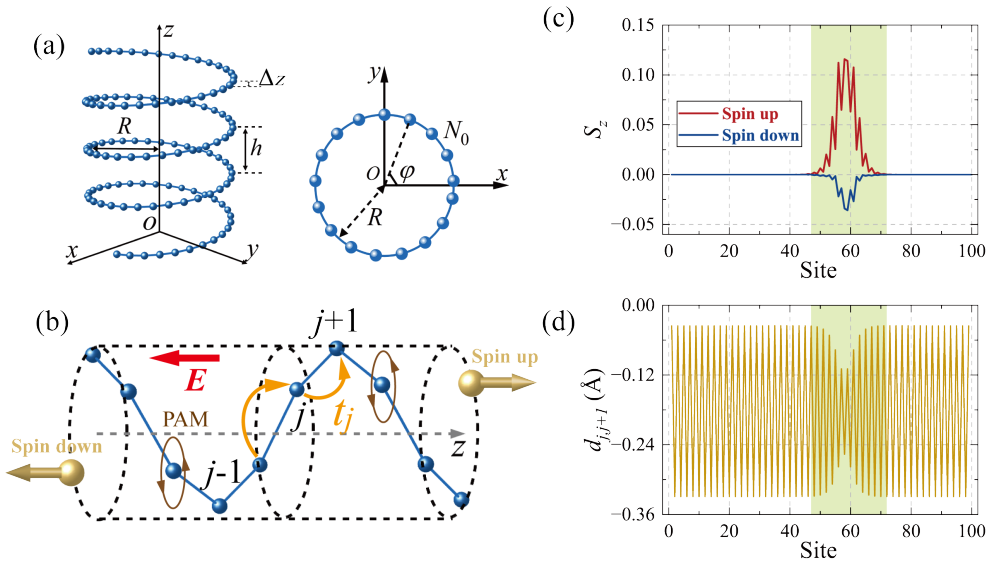

Fig. 1. (a) and (b) The schematic illustrations of the chiral chain model and the spin-dependent polaron transport process. In this model, the helix pitch h, helix radium R, and the z-direction distance between two neighboring sites Δz are assumed as 3.2 nm, 0.7 nm, and $3.2/N_0$ nm,[37] respectively, where N_0 denotes the number of atoms contained within a single helical turn. (c) The spin-density distribution of the static polaron with spin up (red) and spin down (blue). (d) The variation of the bond length between nearest-neighbor sites when the static polaron is generated. All calculations adopt periodic boundary conditions and parameters are presented in the SM.

where $\boldsymbol{S}_j$, $\boldsymbol{L}_j$ are the jth site's electron spin and PAM, respectively; σ_λ ($\lambda = x, y, z$) is the Pauli matrix, and g is the coupling constant. Moreover, it should be mentioned that the exact value of g remains under debate. Prevailing research typically suggests that g should be set in a way that the energy of the ECP term is on the order of meV.[35] Therefore, in subsequent model investigations, we will adopt this criterion as the standard for choosing the parameter value of g.

Considering that the transport in chiral molecules does not occur in isolation but is instead closely interwined with the coupling of surrounding lattice distortions, this process ultimately leads to a spatially localized polaron effect.[40] Consequently, in the subsequent analysis, based on the established existence of a stable polaron state within the system, we will further investigate phenomena associated with PAM during the electric field-driven transport process and its dependence on relevant parameters. Specifically, by assuming band half-filling, we first determine the Peierls-gapped ground state through self-consistent calculations of Eq. (1). Subsequently, an electron is injected into the lowest unoccupied energy band, forming a negatively charged polaron. On this basis, we then incorporate the Peierls phase factor ahead of the hopping term in Eq. (1) to simulate the electric filed-driven effect,[41] which finally result in a time-dependent Hamiltonian $H(t)$. By solving the time-dependent Schrödinger equation, we can obtain the evolution of wave functions for the polaron propagating along the chain. Simultaneously, the lattice motion state can also be derived by solving Newton's equation, and the PAM can be calculated based on these results. The details of the above processes can be found in the Supplemental Materials (SM).

To gain insight into the intrinsic physical mechanisms while avoiding complications arising from the complex details of DNA molecules, we adopt the helical chain model in subsequent calculations. As depicted in Fig. 1(a), the originally intricate DNA base pairs are abstracted as discrete sites along the helical chain, whereas the rigid phosphate backbone is modeled as elastic bonds connecting these sites. Following this, we focus on the generation mechanism of PAM during the chain propagation process of a spin-s electron driven by the electric field, as shown Fig. 1(b). Crucially, this process involves a self-consistent interplay between spin dynamics and lattice responses: The propagating electron induces moving localized lattice deformations through electron–phonon coupling, which in turn stabilizes the formation of a spin-polarized polaron and generate finite PAM. Therefore, to ensure the rigor and validity of the investigations, we start by constructing a stable static polaron. As illustrated in Fig. 1(c), we first present the specific configuration of the static polaron and its corresponding spin density distribution, where the negatively charged polaron is localized between approximately the 47th and 67th sites. Due to the SOC interaction, this polaron predominantly exhibits the state of spin up. Furthermore, the lattice distortions are also demonstrated in Fig. 1(d). To more accurately capture the variations in electron–phonon interaction, we choose the changes in bond lengths of neighboring sites as the quantifiable parameter for assessing lattice distortions. It can be recognized that the distorted region is nearly equivalent in size to the area occupied by the electron, encompassing approximately 20 sites.

We subsequently investigate the polaron transport process under different z-axis direction electric fields. By incorporating the Peierls factor ahead of the electron hopping term between lattice sites, we introduced the effect

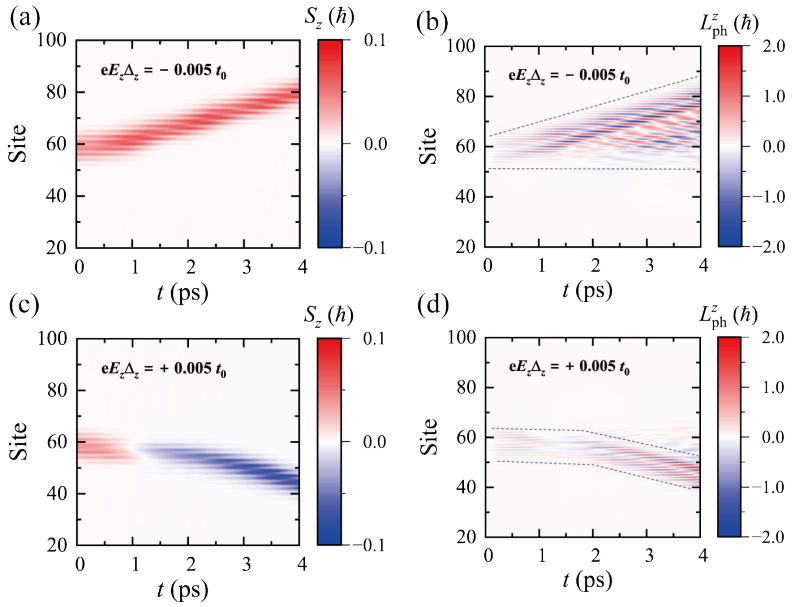

Fig. 2. Time evolutions of spin s^z_j and PAM L^z_j distributions at (a) and (b) $eE_z\Delta z = -0.005t_0$, and (c) and (d) $eE_z\Delta z = 0.005t_0$.

of the external electric field (see section 2 of the SM). To further clarify the specific impacts of the two types of electron–phonon interactions (the conventional one and the ECP) on spin flipping and PAM generation, we first switch off the ECP in the current analysis by setting the coupling constant g to 0. Figure 2 demonstrates the resulting distributions of spin polarization and PAM, as well as their evolution over time. When the external field is applied along the negative z-axis [Figs. 2(a) and 2(b)], the static polaron begins to propagate along the chiral axis. At this stage, the spin polarization remains the initial distribution without flipping, while the spatial distribution of PAM demonstrates a tendency toward non-local diffusion and exhibits complex interference-like fringe patterns. This phenomenon can be further explained by the propagation of lattice waves and their mutual superposition. As the electron with associated local lattice distortions moves along the chain, the position of the polaron can be considered as a new wave source for inducing lattice vibration. Therefore, the overall motion of the lattice can be regarded as the superposition of two components: one being the new lattice response induced by the current polaron, and the other being the passing wave traveling along the chain. Since both components arise from forced vibrations generated by electron hopping, they are coherent. Consequently, when these two components are superimposed, the PAM interference patterns ultimately emerge, as expected in Figs. 2(b) and 2(d). Interestingly, upon reversal of the electric field, not only is spin polarization inversion observed, but the spatial distribution of PAM also demonstrates localized mobility features akin to those of the polaron. This stands in stark contrast to the diffusive behavior of PAM previously observed. The former has been elucidated in prior studies as resulting from the helically shaped electric field induced by SOC. However, the latter, as a distinctive property emerging from the interplay between spin dynamics and lattice responses, has remained unexplored until now.

To further explore the potential underlying mechanism, we subsequently analyze the time dependence of the total spin polarization and PAM under different external field (E) conditions. Additionally, by setting the effective SOC parameters $t_{\rm SO}$ and $t_{\rm SI}$ to zero, we examine the generation of PAM in the absence of spin selection to clarify the relationship between spin selection and PAM generation. Figures 3(a) and 3(b) present the corresponding results with and without spin selection, respectively. One can see that even when spin selection is absent, a nonzero PAM is still induced under polarons driving, which strongly indicates that spin selection is not the underlying cause of the PAM generation. However, it is an undeniable fact that a mutual influence exists between these two proecesses. In the absence of spin selection [Fig. 3(b)], the induced PAM is obviously an odd function of the electric field. Conversely, when spin selection is present, this relationship is disrupted due to the breaking of time-reversal symmetry. As shown in Fig. 3(a), it is obvious that as time evolves, the total PAM exhibits a slight fluctuation in overall value for $eE_z\Delta z = -0.005t_0$ (Δz is the z-direction distance between two neighboring sites), whereas a significant and rapid increase occurs for $eE_z\Delta z = 0.005t_0$. Furthermore, it is noteworthy that when the polaron propagates along the negative z-axis, the total PAM consistently aligns with the positive z-axis. Conversely, when the polaron moves along the positive z-axis, the PAM reverses its direction, which indicates that the existence of a potential dependence between the generated PAM and the chiral structure as well as the direction of polaron motion. In fact, previous studies on the propagation of chiral phonons in chiral materials have included similar discussions on this special dependence, which is further defined as the chiral phonon diode effect.[27] It is reported that when considering phonon transport along the chiral axis, only phonons with angular momentum

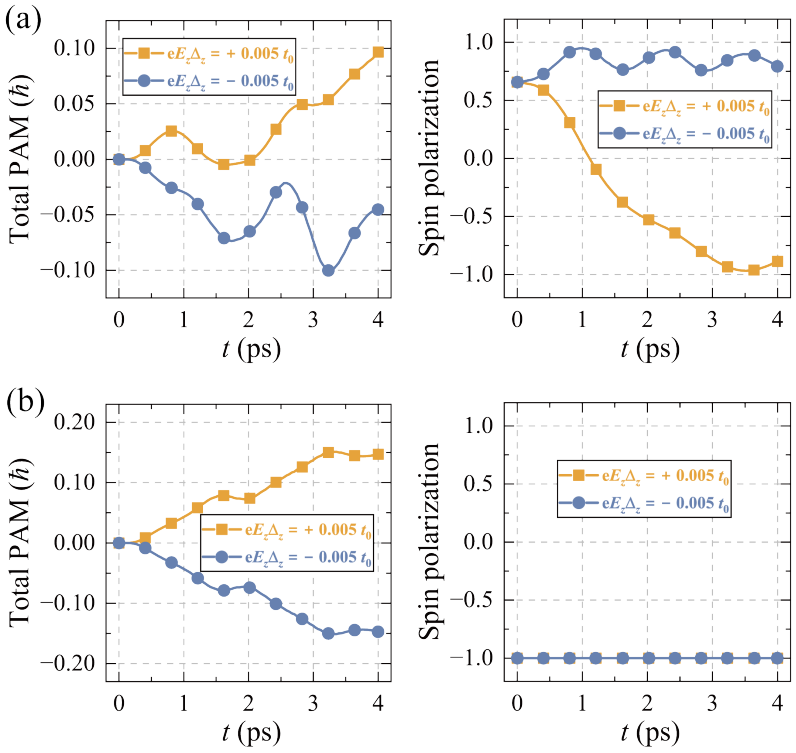

Fig. 3. Time evolution of PAM and spin polarization (a) with spin selection and (b) without spin selection. The left panel illustrates the temporal evolution of PAM, while the right panel depicts the variation in spin polarization. Two distinct driving electric fields acting in opposite directions are taken into account. The brown square line denotes the driving of polaron along the chiral axis, whereas the blue circle line represents the opposite direction of driving.

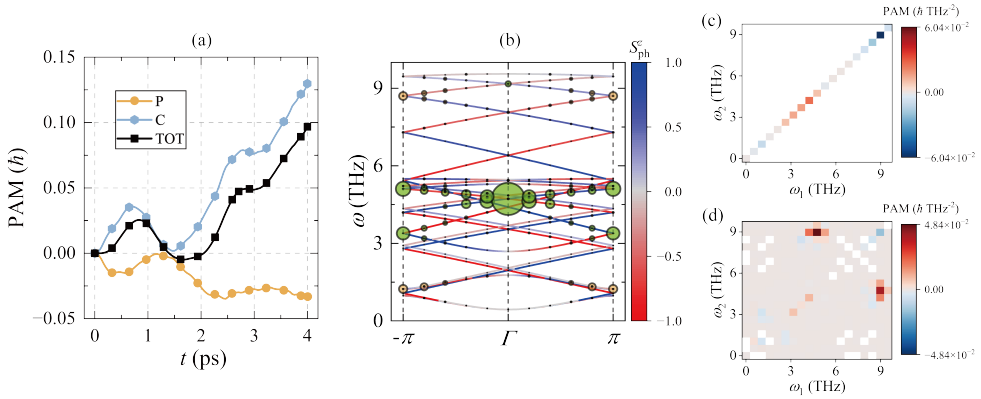

Fig. 4. The origin of PAM at $eE_z\Delta z = 0.005t_0$. (a) The evolution of contributions from the channel ('P', blue, hexagon) and coherence channel ('C', brown, circle) in PAM generation. (b) The phonon spectrum of the chiral chain model. The color gradient indicates the phonon polarization of each mode, with red and blue corresponding to the negatively and positively polarized phonons, respectively. Moreover, the colored circles in the plot represent the phonon modes $(\boldsymbol{q}, s)$ sampled in the calculation; the area of each circle is related to its contribution to induced PAM, while the color distinguishes positive (green) or negative (brown) contributions. Two-dimensional density for the contributions to the induced PAM from (c) the particle channel and (d) the coherence channel.

opposite to the lattice chirality can achieve efficient transport. Based on this, we introduce the lattice Fourier transform of displacement and velocity to systematically investigate the contributions of each phonon mode to the PAM generation. As detailed in section 4 of the SM, we attribute the induced PAM to contributions from two primary channels. The first channel, termed the particle channel, accounts for the angular momentum carried individually by each phonon, consistent with the previously studies.[1] The second channel, arising from the coherent superposition effect among different phonon modes, generates additional PAM and thus referred to as the coherent channel.[42–44]

Figure 4 demonstrates the contributions of the two channels to the PAM when $eE_z\Delta z = 0.005t_0$. Interestingly, we find that the contribution of coherent channel to PAM is opposite in direction to that of particle channel. As the system evolves over time, the contribution of coherent channel gradually becomes dominant [Fig. 4(a)]. This result can be explained by the generation of a new wave source and the superposition effect between waves, as

described in the aforementioned content. Specifically, as a polaron moves, new waves are coherently superimposed with the old waves at all times, thereby significantly amplifying the contribution of the coherent channel. To gain deeper insights into the role of each phonon mode, we further calculate the phonon spectrum, including its associated phonon polarization and the mode contribution ratios as shown in Fig. 4(b). For generality, we focus on the mode contribution at $t = 4$ ps. Due to time-reversal symmetry, the phonon polarization for each mode is an odd function of the wave vector, resulting in no net PAM being generated in the equilibrium state. However, as the movement of the polaron induces lattice deformation and consequently triggers the generation and superposition of lattice waves, even for two modes with opposite phonon polarizations, their contributions to PAM may be identical, exhibiting an even function related to the wave vector. Furthermore, it is evident that the regions with substantial contributions are predominantly concentrated within the 3–6 THz frequency band, with particularly significant contributions arising from the Brillouin zone boundary ($ka = \pm\pi$) and the Γ point. This is because, under the influence of a specific external electric field, only phonon modes with energy that matches the external electric field can be effectively excited. Moreover, given that phonons at the Brillouin zone boundary exhibit relatively high phonon polarization and the coherent superposition effect predominantly manifests as standing waves, the aforementioned distribution phenomenon becomes more comprehensible. We also present the frequency distributions of the contributions from the two channels in Figs. 4(c) and 4(d). We note that in the particle channel, the phonon modes with approximately 9 THz predominantly determines the direction of the final PAM. In contrast, in coherent channels, the superposition effect of phonon modes near 9 THz and near 3 THz is critical in shaping the overall behavior.

As outlined above, we have elucidated the correlation between the generation of PAM and the movement of polarons. This raises an intriguing question: Is the presence of polarons a necessary condition for this process? Alternatively, in general chiral materials, is it feasible to rely solely on electron transport and conventional electron–phonon interactions to induce a finite PAM? To address this question, we conduct an analysis of the evolution of PAM and its space distribution with different electron–phonon coupling constant α. Figure 5(a) illustrates the magnitude of the total PAM, indicating that as the electron–phonon interaction strengthens, the magnitude of PAM initially increases and subsequently decreases. When $\alpha = 140$ meV, the total PAM at $t = 4$ ps is equivalent to that observed when $\alpha = 160$ meV. However, when α further increase to 200 meV, it becomes evident that the induced PAM is comparable in magnitude to the result obtained when $\alpha = 80$ meV, with both values approximating zero. Such non-monotonic dependence on α can be reasonably attributed to the role of electron–phonon interaction in both the formation and migration of polarons. As illustrated in Fig. 5(b), when the electron–phonon interaction is exceedingly weak ($\alpha = 80$ meV), the electron is an extended state characterized by the Bloch wave function, where the probability distribution at each lattice site becomes uniform. In this case, the additional electron-induced forces acting on each site are identical, resulting in uniformly consistent intensity of the PAM interference fringes. Consequently, the positive and negative contributions cancel each other out [Fig. 5(c)], leading to zero PAM. While with the gradual increase in coupling strength, polaron formation begins to occur, where electron exhibits localized distribution

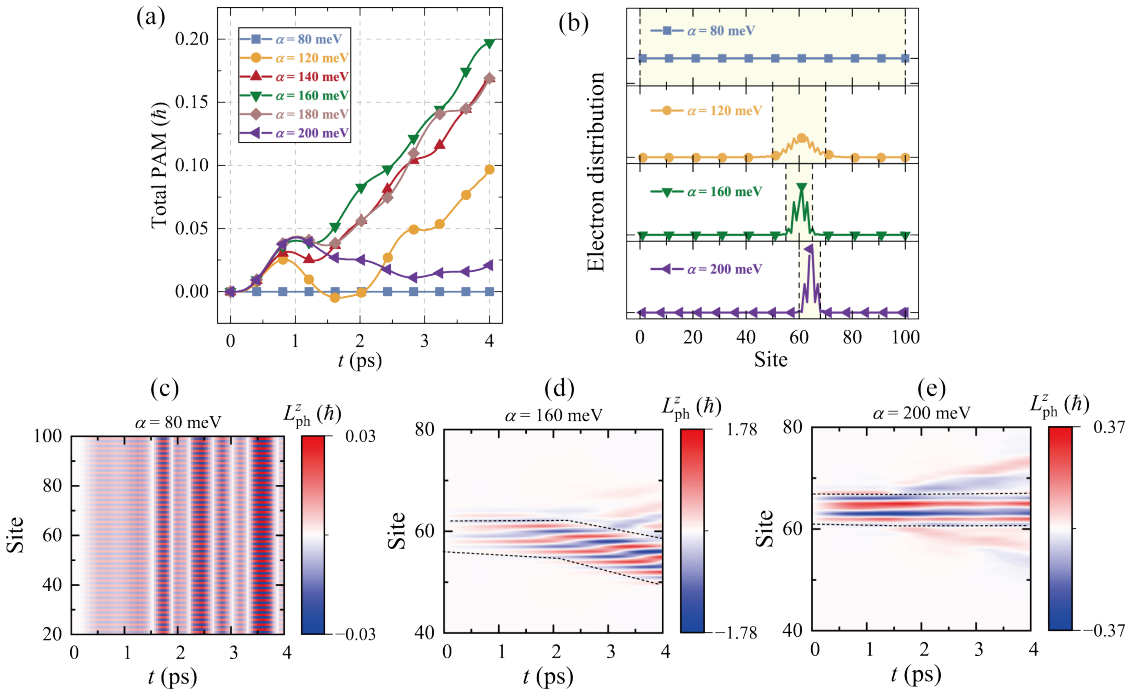

Fig. 5. (a) Time evolutions of total PAM and (b) electron distribution of the polaron at $t = 0$. (c)–(e) The space distributions of total PAM for different α.

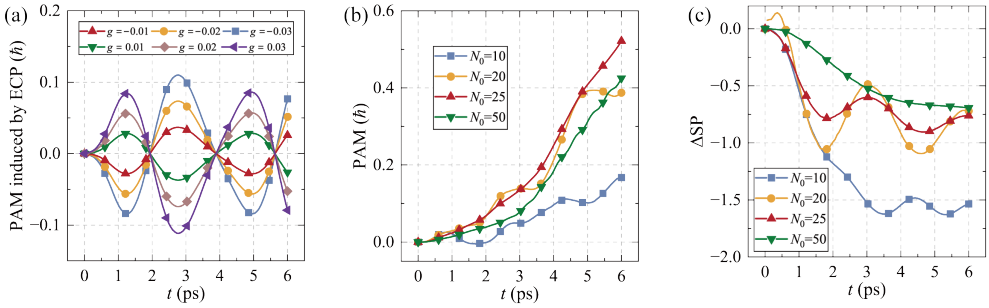

Fig. 6. (a) The time dependence of PAM induced by ECP at different g factors. (b) The time dependence of (b) PAM for different N_0 and (c) the corresponding spin polarization.

characteristics at specific sites and the degree of localization progressively intensifies as α increases. At this stage, the positive and negative PAM can not completely cancel each other out, result in a finite PAM. However, the increase in the degree of localization is also associated with a reduction in polaron mobility. As depicted in Figs. 5(d) and 5(e), it is obvious that the polaron with $\alpha = 200\,\text{meV}$ exhibits a predominantly stationary behavior, in contrast to the case where $\alpha = 160\,\text{meV}$. Therefore, in our model, achieving considerable PAM necessitates the presence of stable polaron and an appropriate interaction intensity.

Next, we investigate the parameter dependence of the generated PAM and the associated spin polarization. Based on the current work, the ECP interaction only leads to the opening of a very small phonon band gap,[33] typically on the order of a few meV. To ensure that the strength of the ECP interaction remains within a physically reasonable range, we vary the control parameter g between -0.03 and 0.03 in our analysis. Figure 6(a) displays the time evolution of PAM at $eE_z\Delta z = 0.005t_0$ with varying ECP strength g. To more intuitively investigate the influence of ECP interactions on the PAM, here we have eliminated the contributions of conventional electron–phonon interactions through the relationship $L_{\text{ph}}^{\text{ECP}} = L_{\text{ph}}^{\text{tot}}(g) - L_{\text{ph}}^{\text{tot}}(0)$. As shown, the additional PAM induced by the ECP interaction exhibits a pronounced near-periodic variation over time. As g varies from 0.01 to 0.03, the fluctuation range progressively increases. Moreover, the sign of g determines the trend of the fluctuation change. These effects can be attributed to the specific form of ECP interaction employed in this model, which arise from the instantaneous coupling between spin and PAM at the same site. Given the mismatch between the time scales of lattice relaxation and polaron motion, the system can not feel the ECP interaction when the polaron moves too rapidly. Additionally, the presence of PAM diffraction patterns further reduces the influence of ECP interaction. Consequently, it is reasonable to infer that during the entire motion process, the dominant contribution of ECP interaction stems from the electric field excitation of a stationary polaron during the initial stage. As a result, the induced PAM does not exhibit any dependence on spin flipping and consistently repeats the initial contribution, as expected in Fig. 6(a). Subsequently, we discuss the influence of structural periodicity. Figures 6(b) and 6(c) illustrate the evolution of PAM and spin polarization at different N_0. To more precisely capture the variation in spin polarization, we define ΔSP as the change in spin polarization relative to its initial value. The results demonstrate that as N_0 increases, the induced PAM progressively rises to a stable value, whereas the change in spin polarization exhibits an opposite trend. This is because, for phonons, increasing the number of atoms within the period promote the emergence of additional chiral modes, thereby enhancing the generation of PAM. However, for polarons, an increase in the number of sites within a helical turn reduces the difference in helix angles between the neighbor sites, which further weakens the helical characteristics of the local structure and thus is not conducive to the spin inversion. Thus, a relatively appropriate N_0 is of great significance for both the generation of PAM and spin dynamics.

3. Experimental Proposal. We finally propose a feasible experiment to measure the induced PAM during the polaron transport process. Since the PAM characterizes the local rotation of microscopic atoms within a picosecond time scale, it is challenging to directly observe it with current experimental methods. Nevertheless, based on the conservation of angular momentum, the generated PAM can be reflected through changes in other forms of angular momentum. In this scenario, when a finite PAM occurs, the DNA helical chain may undergo rigid body rotation, similar to the Einstein–de Haas effect.[45] Thus, by employing highly sensitive instruments such as torsion balance systems capable of detecting minute rotational displacements and measuring the associated torque, we anticipate being able to quantify the magnitude of the induced PAM. Notably, a recent study[46] has successfully observed PAM in a chiral tellurium (Te) system using a similar methodology. This achievement not only validates the feasibility of theoretical predictions, but also provides important experimental references and technical support for us to carry out similar experiments in DNA-based biomolecular materials.

4. Summary. We thoroughly investigate the generation mechanism of PAM during the transport of a spin-polarized polaron. By employing the helical chain model, we successfully reproduce the spin selection phenomenon observed in DNA molecules and conduct a systematic analysis of the time evolution of the induced PAM. It is found that the direction of induced PAM is intrinsically linked to the movement direction of the polaron. Upon reversal of the driving field, the PAM also reverses accordingly.

Thus, our work offers a promising avenue for effectively modulating PAM via an external field. Additionally, the conventional electron–phonon interaction is found to play a pivotal role in the generation of PAM, not only strongly correlating spin dynamics with lattice distortion but also affecting the size and mobility of polarons. To achieve efficient PAM generation, we suggest the conductive systems with polarons as carriers, such as biopolymer materials, could serve as potential ideal platforms. Furthermore, we also investigate the influence of ECP interaction and structural periodicity. Due to the localized nature of polarons, the ECP interaction contributes less significantly compared to the conventional electron–phonon interaction, introducing only minor near-periodic fluctuations over time in the PAM. While for the structural periodicity, increasing the number of atoms within a single helix is found to enhance the generation of PAM to a certain extent due to the increased phonon modes. However, this also reduces the spin flipping by decreasing local structural chirality. Therefore, to balance both spin flipping and the PAM generation, selecting an appropriate N_0 is critically important.

Recent studies[47–49] have conclusively demonstrated that the PAM has a significant impact on the electronic properties. However, the challenge of pre-determining the existence of PAM in materials remains unresolved in these investigations. Our work addresses this critical issue by successfully generating PAM through the application of achievable electric fields in conjunction with naturally occurring biological DNA molecules. It is anticipated that the induced PAM within DNA molecules could, in turn, lead to changes in their electronic properties. This, thereby, potentially provides a promising avenue for experimental verification. Nonetheless, due to the current model's reliance on the single-electron approximation, further exploration of these processes will be undertaken in our future research. Overall, our work not only offers novel insights for the design of related phonon-based devices but also establishes a fresh paradigm for both experimental and theoretical investigations in this field.

Acknowledgements. This work was supported by the National Key R&D Project from Ministry of Science and Technology of China (Grant No. 2022YFA1203100), the National Natural Science Foundation of China (Grant No. 52350088), the Department of Science and Technology of Jiangsu Province (Grant No. BK20220032), and the Postgraduate Research & Practice Innovation Program of Jiangsu Province (Grant No. KYCX24_1797).

References

[1] Zhang L and Niu Q 2014 *Phys. Rev. Lett.* **112** 085503
[2] Zhang L and Niu Q 2015 *Phys. Rev. Lett.* **115** 115502
[3] Zhang T and Murakami S 2022 *Phys. Rev. Res.* **4** L012024
[4] Hamada M, Minamitani E, Hirayama M, and Murakami S 2018 *Phys. Rev. Lett.* **121** 175301
[5] Park S and Yang B J 2020 *Nano Lett.* **20** 7694
[6] Davies C S, Fennema F G N, Tsukamoto A, Razdolski I, Kimel A V, and Kirilyuk A 2024 *Nature* **628** 540
[7] Pandey T, Polanco C A, Cooper V R, Parker D S, and Lindsay L 2018 *Phys. Rev. B* **98** 241405
[8] Romao C P 2019 *Phys. Rev. B* **100** 060302
[9] Grissonnanche G, Thériault S, Gourgout A, Boulanger M E, Lefrançois E, Ataei A, Laliberté F, Dion M, Zhou J S, Pyon S, Takayama T, Takagi H, Doiron-Leyraud N, and Taillefer L 2020 *Nat. Phys.* **16** 1108
[10] Mella J D, Calvo H L, and Foa Torres L E F 2023 *Nano Lett.* **23** 11013
[11] Rini M, Tobey R a, Dean N, Itatani J, Tomioka Y, Tokura Y, Schoenlein R W, and Cavalleri A 2007 *Nature* **449** 72
[12] Hernandez F G G, Baydin A, Chaudhary S, Tay F, Katayama I, Takeda J, Nojiri H, Okazaki A K, Rappl P H O, Abramof E, Rodriguez-Vega M, Fiete G A, and Kono J 2023 *Sci. Adv.* **9** eadj4074
[13] Nova T F, Cartella A, Cantaluppi A, Först M, Bossini D, Mikhaylovskiy R V, Kimel A V, Merlin R, and Cavalleri A 2017 *Nat. Phys.* **13** 132
[14] Cheng B, Schumann T, Wang Y, Zhang X, Barbalas D, Stemmer S, and Armitage N P 2020 *Nano Lett.* **20** 5991
[15] Luo J, Lin T, Zhang J, Chen X, Blackert E R, Xu R, Yakobson B I, and Zhu H 2023 *Science* **382** 698
[16] Wu F, Bao S, Zhou J, Wang Y, Sun J, Wen J, Wan Y, and Zhang Q 2023 *Nat. Phys.* **19** 1868
[17] Komiyama H and Murakami S 2021 *Phys. Rev. B* **103** 214302
[18] Schaack G 1976 *J. Phys. C: Solid State Phys.* **9** L297
[19] Anastassakis E, Burstein E, Maradudin A A, and Minnick R 1972 *J. Phys. Chem. Solids* **33** 519
[20] McLellan A G 1988 *J. Phys. C: Solid State Phys.* **21** 1177
[21] Ray T and Ray D K 1967 *Phys. Rev.* **164** 420
[22] Ioselevich A S and Capellmann H 1995 *Phys. Rev. B* **51** 11446
[23] Rückriegel A and Duine R A 2020 *Phys. Rev. Lett.* **124** 117201
[24] Mankovsky S, Polesya S, Lange H, Weißenhofer M, Nowak U, and Ebert H 2022 *Phys. Rev. Lett.* **129** 067202
[25] Choi I H, Jeong S G, Song S, Park S, Shin D B, Choi W S, and Lee J S 2024 *Nat. Nanotechnol.* **19** 1277
[26] Tauchert S R, Volkov M, Ehberger D, Kazenwadel D, Evers M, Lange H, Donges A, Book A, Kreuzpaintner W, Nowak U, and Baum P 2022 *Nature* **602** 73
[27] Chen H, Wu W, Zhu J, Yang Z, Gong W, Gao W, Yang S A, and Zhang L 2022 *Nano Lett.* **22** 1688
[28] Kim K, Vetter E, Yan L, Yang C, Wang Z, Sun R, Yang Y, Comstock A H, Li X, Zhou J, Zhang L, You W, Sun D, and Liu J 2023 *Nat. Mater.* **22** 322
[29] Ohe K, Shishido H, Kato M, Utsumi S, Matsuura H, and Togawa Y 2024 *Phys. Rev. Lett.* **132** 056302
[30] Ray K, Ananthavel S P, Waldeck D H, and Naaman R 1999 *Science* **283** 814
[31] Göhler B, Hamelbeck V, Markus T Z, Kettner M, Hanne G F, Vager Z, Naaman R, and Zacharias H 2011 *Science* **331** 894
[32] Naaman R, Paltiel Y, and Waldeck D H 2019 *Nat. Rev. Chem.* **3** 250
[33] Gao Y, Pan Y, Zhou J, and Zhang L 2023 *Phys. Rev. B* **108** 064510
[34] Fransson J 2023 *Phys. Rev. Res.* **5** L022039
[35] Yao D, Matsuo M, and Yokoyama T 2024 *Appl. Phys. Lett.* **124** 162603
[36] Zhang L L, Qin W, Xie S J, and Qu F 2020 *Phys. Rev. B* **102** 214303
[37] Gutierrez R, Díaz E, Naaman R, and Cuniberti G 2012 *Phys. Rev. B* **85** 081404
[38] Geilhufe R M 2022 *Phys. Rev. Res.* **4** L012004
[39] Funato T, Matsuo M, and Kato T 2024 *Phys. Rev. Lett.* **132** 236201
[40] Xie S J, Mei L M, and Lin D L 1994 *Phys. Rev. B* **50** 13364

[41] Liu X, Gao K, Fu J, Li Y, Wei J, and Xie S 2006 *Phys. Rev. B* **74** 172301
[42] Simoncelli M, Marzari N, and Mauri F 2019 *Nat. Phys.* **15** 809
[43] Caldarelli G, Simoncelli M, Marzari N, Mauri F, and Benfatto L 2022 *Phys. Rev. B* **106** 024312
[44] Zhong J, Sun H, Pan Y, Wang Z, Xu X, Zhang L, and Zhou J 2023 *Phys. Rev. B* **107** 125147
[45] Viktor Ya F 1979 *Sov. Phys. Usp.* **22** 580
[46] Zhang H, Peshcherenko N, Yang F, Ward T Z, Raghuvanshi P, Lindsay L, Felser C, Zhang Y, Yan J Q, and Miao H 2025 *Nat. Phys.*
[47] Medina Dueñas J, Calvo H L, and Foa Torres L E F 2022 *Phys. Rev. Lett.* **128** 066801
[48] Geilhufe R M and Hergert W 2023 *Phys. Rev. B* **107** L020406
[49] Zhang S, Luo K, and Zhang T 2024 *npj Comput. Mater.* **10** 264